



Surface reconstruction and charge distribution enabling Ni/W₅N₄ Mott-Schottky heterojunction bifunctional electrocatalyst for efficient urea-assisted water electrolysis at a large current density

Yumin Zhou ^{a,1}, Bingxian Chu ^{a,1}, Zhengjian Sun ^a, Lihui Dong ^{a,b}, Fan Wang ^a, Bin Li ^{a,b}, Minguang Fan ^{a,b,*}, Zhengjun Chen ^{a,**}

^a Guangxi Key Laboratory of Electrochemical Energy Materials, School of Chemistry and Chemical Engineering, Guangxi University, Nanning 530004, PR China

^b Guangxi Key Laboratory of Petrochemical Resource Processing and Process Intensification Technology, Guangxi University, Nanning 530004, PR China



ARTICLE INFO

Keywords:

Urea-assisted water electrolysis
Urea oxidation reaction
Hydrogen evolution reaction
Bifunctional electrocatalyst
Mott-Schottky heterojunction

ABSTRACT

Urea-assisted water electrolysis is regarded as an energy-efficient strategy for hydrogen production, but its potential use is still limited by sluggish kinetics in both anodic urea oxidation reaction (UOR) and cathodic hydrogen evolution reaction (HER). Herein, we report the facile synthesis of nickel foam (NF) supported Ni/W₅N₄ Mott-Schottky heterojunction nano-microspheres as a highly active catalyst for both UOR and HER using a hydrothermal method followed by nitridation treatment. The as-prepared Ni/W₅N₄/NF catalyst with high electrochemically active surface area would reconstruct under oxidizing condition to form nickel tungsten oxyhydroxides to efficiently drive UOR, with a potential of only 1.34 V (versus reversible hydrogen electrode) at 10 mA cm⁻². Impressively, thus-prepared catalyst benefited from charge redistribution only required an overpotential of 25 mV at 10 mA cm⁻² for HER. In particular, the Ni/W₅N₄/NF catalyst couple used for urea-assisted water electrolysis just needed a cell voltage of 1.77 V at 1000 mA cm⁻².

1. Introduction

Hydrogen is a clean and sustainable energy carrier, and its coupled application with renewable sources is expected to alleviate the energy crisis and environmental problems [1–3]. Water electrolysis powered by green energy is an environmentally friendly way for hydrogen production [4–7]. However, the energy efficiency of this reaction is severely restricted by the anodic oxygen evolution half-reaction (OER) with a high thermodynamic equilibrium potential of 1.23 V [8,9]. Urea oxidation reaction (UOR, CO(NH₂)₂ + 6OH⁻ → N₂ + 5H₂O + CO₂) has been recently regarded as an ideal alternative to OER owing to its ultra-low theoretical potential with only 0.37 V [10,11]. Meanwhile, UOR also provides a potential solution for purification of urine-containing wastewater, and its products (N₂ and CO₂) could further avoid hazardous H₂/O₂ explosions [12–15]. Nevertheless, its large-scale application was greatly hindered by the intrinsically sluggish kinetics, which may originate from its complex six-electron reaction

process and multistep adsorption/desorption of reactants/products. Crucial to overcoming these kinetic issues is to develop advanced electrocatalysts for the UOR [16–18]. In addition, the rational design of catalysts with high activity for the both UOR and cathodic hydrogen evolution half-reaction (HER) is greatly desirable for the urea-assisted water electrolysis to hydrogen production. In that case, the catalysts could be integrated in a same electrolyte, which would in-turn simplify the electrolyzer and reduce the manufacturing cost.

Noble metal (like Ru, Pt) based materials are well-known as the effective catalysts for the UOR and HER, yet also supplanted for its inherent disadvantages of high cost and the scarcity [19,20]. In the past decades, efforts towards the development of cost-efficient catalysts have increased substantially. As a result, a variety of non-precious metal-based materials such as phosphides [21,22], sulfides [13,14], selenides [23], and (hydr)oxides [24–26] have been identified as active UOR/HER catalysts. Among them, transition metal nitrides (TMNs) have exhibited great application potential owing to their advantages in high corrosion

* Corresponding author at: Guangxi Key Laboratory of Electrochemical Energy Materials, School of Chemistry and Chemical Engineering, Guangxi University, Nanning 530004, PR China.

** Corresponding author.

E-mail addresses: fanmg@gxu.edu.cn (M. Fan), zjchen@gxu.edu.cn (Z. Chen).

¹ These authors contributed equally to this work.

resistance, good electrical conductivity, and intriguing UOR/HER bifunctional performance [27–29]. Meanwhile, the employment of several strategies (like architecture engineering, elements doping, and heterostructure engineering) also have resulted in remarkable improvements of the activity of these versatile catalysts, as exemplified by the studies on the Ce-Ni₃N [29], V-Ni₃N [30], Ni₃N/Ni_{0.2}Mo_{0.8}N [31], and Ni_xFeN/Ni₃N [32] catalysts. But based on the previous studies, the surface of TMNs used for UOR typically reconstructed into metal oxyhydroxides (like NiOOH, CoOOH), which may act as the true catalytically active sites for UOR [33–35]. Even so, few strategies on the direct synthesis of these metal oxyhydroxides have been reported, and the existing strategies easily affect the active site exposure [36,37]. The TMNs were generally regarded as the precatalysts for surface reconstruction to provide the massive catalytically active sites and as a key role in conducting electricity [30,32,38]. In this sense, a rational design of TMNs with high conductivity and specific surface area would be an excellent choice for the UOR catalysts.

Recently, Mott-Schottky heterojunction engineering has emerged as a new powerful modified strategy [39–41]. It was reported that the application of this manipulation would result in the charge redistribution of the catalysts at the heterointerface to form built-in electric field, which give rise to effectively promote the electron transfer [14,42]. Additionally, the Mott-Schottky heterojunction materials as a pre-catalyst under oxidation condition would form the metal oxyhydroxides on the surface, providing a large number of UOR active sites. Moreover, the charge redistribution of catalysts could result in the enrichment of excessive electron on the metal surface, which would in turn accelerate the HER process [12,43,44]. This strategy perfectly meets the requirements for the design of highly efficient UOR/HER bifunctional catalysts. In practice, several high-performance catalysts have been yielded by application of this novel strategy, such as NiS/MoS₂ [42] and Ni/NiO@NC [45] catalysts. But in a general view, the activity and long-term stability of the most existed inexpensive UOR/HER catalysts have not yet met the requirement of industrial applications. The TMNs-based Mott-Schottky heterostructure catalysts for the both UOR and HER remain to be explored, especially used in the industrial condition at large current density.

In this work, a nickel foam (NF) supported Ni/W₅N₄ Mott-Schottky heterojunction nano-microspheres as a highly active catalyst for both UOR and HER was fabricated by typical hydrothermal and subsequent controllable nitridation treatments. Our study showed that the Ni/W₅N₄/NF catalyst respectively requires only 1.34 and 1.60 V (versus Reversible Hydrogen Electrode, RHE) to obtain the current densities of 10 and 1000 mA cm⁻² to drive the UOR. This activity outperformed that of most reported non-precious UOR catalysts. Furthermore, the as-prepared Ni/W₅N₄/NF catalyst also possesses satisfied HER activity with an overpotential of only 25 mV at 10 mA cm⁻². When Ni/W₅N₄/NF catalyst is used as both the anode and cathode for urea-assisted water electrolysis, the cell voltage only needs 1.33 and 1.77 V to achieve 10 and 1000 mA cm⁻², respectively. Additionally, the high-efficient urea-assisted hydrogen production system also shows excellent stability over 200 h, highlighting its potential for industrial applications.

2. Experimental

2.1. Preparation of the catalyst

Firstly, the precursor was prepared by a similar hydrothermal method reported by our group [46]. A piece of Ni foam (NF, ≥99%, ~1.8 mm in thick, Kunshan Jiayisheng Electronic Co., Ltd) with area of 1 cm × 4 cm was ultrasonically cleaned in 3 M hydrochloric acid (HCl, 36–38%, Chengdu Kelong Chemical Co., Ltd) solution, ethanol (C₂H₆O, 99.5%, Sichuan Xilong Science Co., Ltd), and deionized (DI) water for 15 min each. Then 1 mmol nickel nitrate hexahydrate (Ni(NO₃)₂·6H₂O, 98%, Guangdong Guanghua Sci-Tech Co., Ltd) and 0.25 mmol ammonium metatungstate hydrate ((NH₄)₆H₂W₁₂O₄₀·xH₂O, 99%, Aladdin)

were dissolved in 30 mL DI water and subsequently transferred into a Teflon lined stainless autoclave. After placing the cleaned NF, the autoclave was sealed and subsequently maintained at 180 °C for 6 h in an electric oven. After the autoclave cooled down to room temperature, the product was washed several times with DI water and dried overnight at 60 °C to get the Ni₄W₆O₂₁(OH)₂·4H₂O/NF precursor (named hydrothermal sample). Finally, the hydrothermal sample was annealed at 500 °C for 2 h under high-purity NH₃ atmosphere to obtain the target sample.

2.2. Materials characterization

The morphology and microstructures of the catalysts were characterized by field-emission scanning electron microscope (FE-SEM, SU8220, Hitachi) and transmission electron microscope (TEM, Talos F200S, FEI). The phases of the catalysts were characterized by X-ray diffraction (XRD, DX-2700A, Haoyuan Instrument Co., Ltd. Cu K_α radiation). The chemical bonds and elemental composition of the catalysts were carried out by X-ray photoelectron spectroscopy (XPS, ESCALAB 250XI+, Thermo Fisher Scientific). The XPS peak positions were calibrated to the C 1s line (at 284.8 eV) of adventitious hydrocarbon. In the XPS depth profile analysis, the Ar⁺ ion beam energy was adjusted to 1000 eV and the etch rate was around 0.2 nm s⁻¹. Raman spectra were performed on a Laser Raman Spectrometer equipment (inVia Reflex, Renishaw) with 532 nm excitation wavelength.

2.3. Electrochemical measurements

Electrochemical tests were carried out on the electrochemical workstation WaveDriver 100 (Pine Research Instrumentation, Inc.) in a typical three-electrode cell. The NF-supported catalysts were directly used as working electrode, the platinum foil (for UOR and OER measurement) or the graphite rod (for HER measurement) was used as counter electrode, and the Hg/HgO electrode (with 1.0 M KOH) was used as reference electrode. All the potentials reported in our manuscript were converted to RHE scale according to the equation:

$$E_{\text{RHE}} = E_{\text{Hg/HgO}} + 0.924 \text{ V} \quad (1)$$

The polarization curves were recorded using linear sweep voltammetry (LSV) method by scanning the potential at a scan rate of 1 mV s⁻¹. Before the UOR test, the catalysts were further activated in 1.0 M KOH with 0.5 M urea solution through continuous cyclic voltammetry (CV) cycles at a scan rate of 50 mV s⁻¹ in a potential range of 0.076 V (vs. Hg/HgO) to 0.776 V (vs. Hg/HgO), until the curves overlapped. The long-term stability was measured by chronopotentiometric (CP) method at different target current densities. Another electrochemical stability test was performed by CV cycles at the scan rate of 100 mV s⁻¹. All the potentials were given with 90% iR compensation by the following equation:

$$E_{\text{corrected}} = E_{\text{uncorrected}} - I \times R_{\text{measured}} \quad (2)$$

The electrochemical impedance spectroscopy (EIS) was recorded using the CHI660E (CH Instruments, Inc.) electrochemical workstation in a frequency range from 0.1 MHz to 0.1 Hz with an AC amplitude of 5 mV. The electrochemically active surface area (ECSA) was estimated by measuring the double-layer capacitance (C_{dl}) with the CV method in 0.15 M TBA-PF₆/CH₃CN solution [47,48]. The specific activity of the catalysts was normalized by their ECSA, and the ECSA was calculated by the following equation:

$$\text{ECSA} = C_{\text{dl}} / C_s \quad (3)$$

where C_{dl} is the double layer capacitance, and C_s is the specific capacitance. Faradaic efficiency (FE) was calculated by comparing the theoretical amount with the measured amount of H₂ and O₂ gas with the typical water drainage method.

3. Result and discussion

3.1. Synthesis and characterization

As diagrammatically shown in Fig. 1, the three-dimensional Ni/W₅N₄ electrocatalyst was synthesized by a conventional two-step method. First, the precursor was self-supported on NF substrate by a hydrothermal method. Then, the synthesized hydrothermal product was nitrogenized in high-purity ammonia at elevated temperatures to obtain the target sample. The optimal annealing temperature was determined to be 500 °C by the control experiments (Fig. S1).

The FE-SEM image (Fig. 2a) displayed the unique nano-microspheres structure with diameters of 5–10 μm were observed on the surface of the hydrothermal sample. Numerous nano-microspheres were stacked on the NF surface by a special growth pattern. The high-resolution image (Fig. 2b) further revealed that the nano-microspheres were uniformly accumulated by a large number of nanorods with diameters ranging from 15 to 50 nm and lengths ranging from 0.1 to 10 μm. The SEM images of the nitrided sample (Figs. 2d and 2e) exhibited the same microstructure as the hydrothermal sample, indicating that the morphology was unaffected by nitridation treatment. To confirm the crystal structures of the catalysts grown on the NF surface, both the hydrothermal and nitrided samples were separated by ultrasonic method and characterized by XRD to avoid the interference of the substrate. As shown in Fig. 2c, the result of the hydrothermal sample corresponded perfectly to standard cubic Ni₄W₆O₂₁(OH)₂·4H₂O (JPCDS No. 47-0143) with high crystallinity. After nitridation treatment, the diffraction peaks of the sample could be identified as cubic metal Ni (JPCDS No. 87-0712) and hexagonal W₅N₄ (JPCDS No. 65-4761) phases, indicating the successful preparation of Ni/W₅N₄ materials on NF. The low-resolution TEM image of the nitrided sample (Fig. 2f) clearly showed the dispersed nanorods structure, which is consistent with the SEM results. The SAED pattern (Fig. 2g) showed a series of concentric circles corresponding to the (105) and (101) planes of W₅N₄, and the (111) plane of Ni, further confirming the formation of Ni and W₅N₄ phases. The high-resolution transmission electron microscope (HRTEM) of Fig. 2h and 2i showed the clear lattice fringes and abundant interfaces in the nitrided sample. Specifically, the lattice fringes with the spacing of 0.247 nm and the spacing of 0.203 nm was clearly indexed to the (101) plane of W₅N₄ and the (111) plane of Ni, respectively. The

heterointerface between the Ni and W₅N₄ phases was marked by dotted arrow in Fig. 2i, certifying the formation of heterojunction. Additionally, the magnified area marked by yellow circles in Fig. 2h also clearly present the existence of the interface (Fig. S2b and S2c in the Supporting Information).

The nitrided sample was characterized by XPS to determine the chemical state of the elements. The high-resolution spectrum of Ni 2p_{3/2} of Ni/W₅N₄ (Fig. 3a) showed the typical signal of metallic Ni at the binding energy (BE) of 852.8 eV (Ni 2p_{3/2}), and the signal at 856.2 eV can be assigned to the Ni–O bond generated by inevitable surface oxidation [49–51]. Additionally, our XPS depth profile analysis exhibited that the valence state of Ni mainly existed as Ni⁰ and the Ni–O signal decreased obviously when the Ni/W₅N₄ sample was exposed to an Ar⁺ beam for etching ~20 nm (Fig. S3). This, together with the observation of obvious diffraction peaks of metallic Ni from XRD result (Fig. 2c), corroborated that the Ni–O signal of Ni/W₅N₄ sample should be derived from the surface oxidation of metallic Ni upon air exposure. The W 4f spectrum of Ni/W₅N₄ (Fig. 3b) exhibited the double W–N signals at the BE of 33.7 eV (W 4f_{7/2}) and 35.7 eV (W 4f_{5/2}), while the W–O signals derived from the inevitable oxidation were located at 36.1 and 38.0 eV [52–54]. As shown in Fig. 3c, the N spectrum of Ni/W₅N₄ proved the introduction of N element. The signal with BE at 397.3 eV can be attributed to the W–N bond in Ni/W₅N₄, while the peaks at 399.2 and 401.3 eV can be ascribed to the N–H groups of adsorbed NH₃ and the N–O species, respectively. These results were consistent with conclusions of XRD and TEM analysis, further verifying the formation of Ni/W₅N₄. Moreover, it is worth noting that the BE of metallic Ni 2p_{3/2} in Ni/W₅N₄ possessed positive shift compared with that of the pure metal Ni (852.6 eV) (Fig. 3a). At the same time, comparing with the pure W₅N₄ species, the W–N bond signal of W 4f of Ni/W₅N₄ similarly showed obviously positive shift (Fig. 3b), while the N–W bond signal of N 1s exhibited the negative shift (Fig. 3c). Such results clearly indicate the electron transfer from metallic Ni to W₅N₄ phase, further confirming the formation of Ni/W₅N₄ Mott–Schottky heterojunction. The heterostructure would be expected to accelerate both the UOR and HER as stated below.

3.2. Catalytic performance

The evaluation of the UOR activity for the as-prepared catalysts was performed in 1 M KOH electrolyte containing 0.5 M urea using a typical three-electrode electrochemical system. Fig. 4a showed the comparison of the LSV curves of the Ni/W₅N₄/NF, commercial RuO₂/NF, W₅N₄/NF, hydrothermal samples, and bare NF. It can be seen that the Ni/W₅N₄/NF sample exhibits comparable UOR activity to the commercial RuO₂ catalyst, with a potential of only 1.34 V (vs. RHE) at the current density of 10 mA cm⁻², which is much lower than that of other comparative samples. Impressively, the Ni/W₅N₄/NF catalyst can drive a large current density of 1000 mA cm⁻² with a low potential of 1.60 V (vs. RHE), implying its high prospects for industrial application. This satisfactory activity of Ni/W₅N₄/NF is also superior to that of most recently reported materials for UOR (Table S1). The activity advantage of Ni/W₅N₄/NF catalyst relative to the contrast samples was further reflected on the results of the fitted Tafel slopes from the LSV curves. As seen in Fig. 4b, the Tafel slopes of the Ni/W₅N₄/NF catalyst (35.8 mV dec⁻¹) was much smaller than those of RuO₂/NF (87.6 mV dec⁻¹), W₅N₄/NF (74.9 mV dec⁻¹), hydrothermal sample (90.6 mV dec⁻¹), and bare NF (141.7 mV dec⁻¹). The smaller Tafel slope indicated a faster catalytic kinetic on the surface of Ni/W₅N₄/NF catalyst than others. The remarkably improved UOR activity of Ni/W₅N₄/NF catalyst over the contrast samples should be partly attributed to the Ni/W₅N₄ Mott–Schottky heterojunction. Such a structure may promote the formation of Janus-type charge distribution of the catalysts, which results in the continuous electron transfer and greatly accelerate UOR kinetic of Ni/W₅N₄/NF catalyst [19,29,48].

As a comparison, the OER catalytic activity of the Ni/W₅N₄/NF catalyst was further tested in 1 M KOH without the addition of urea. As

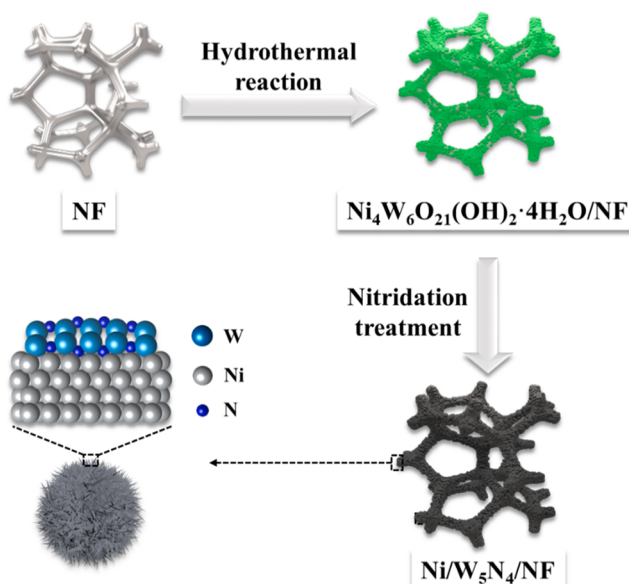


Fig. 1. Schematic flow diagram for the fabrication of the Ni/W₅N₄/NF electrocatalyst.

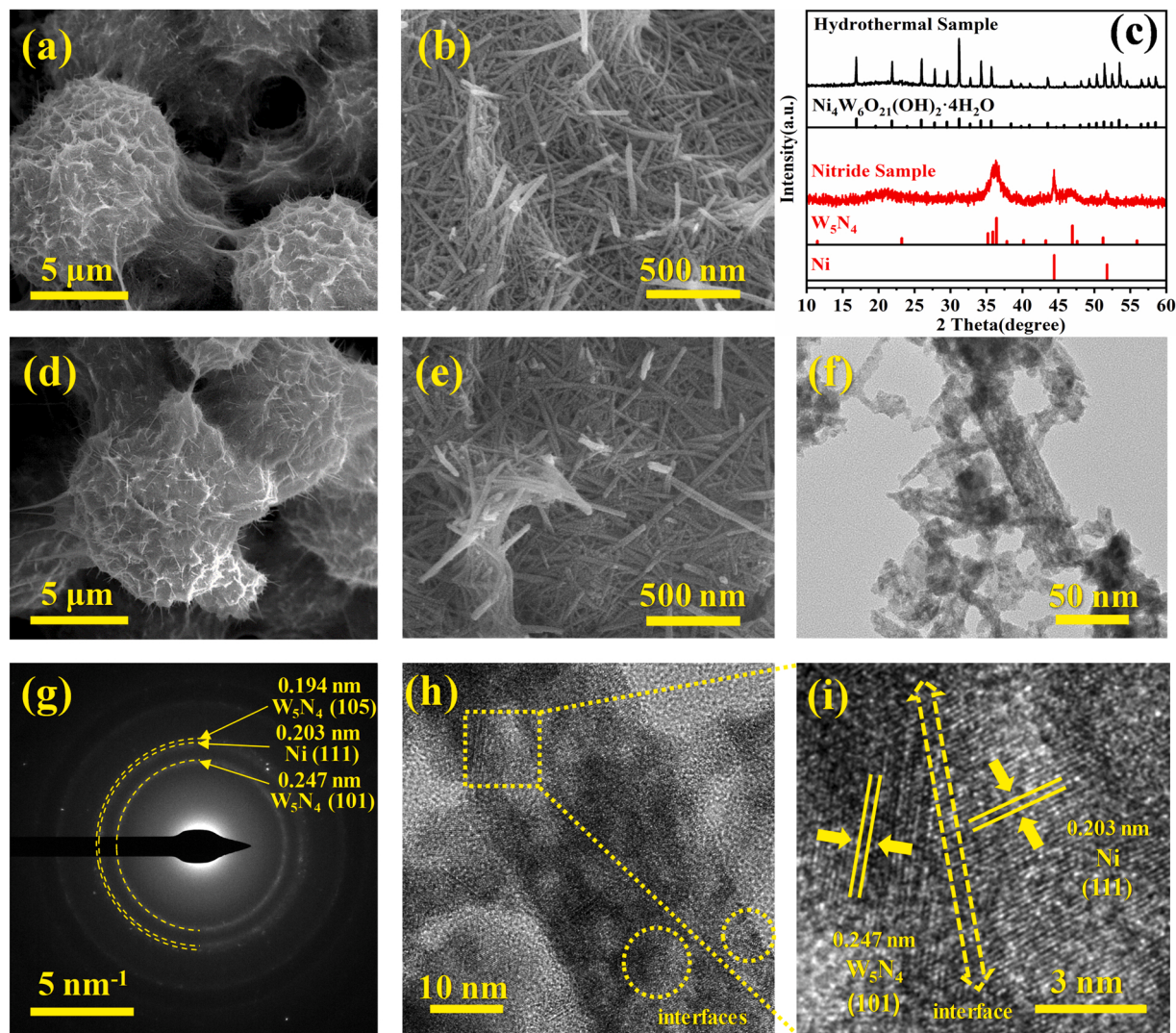


Fig. 2. (a,b) SEM images of the hydrothermal samples. (c) XRD results of hydrothermal and nitrided samples. (d,e) SEM images of the nitrided sample. (f,g) TEM image and SAED pattern of the nitrided sample. (h,i) HRTEM image of the nitrided sample with marked heterointerfaces.

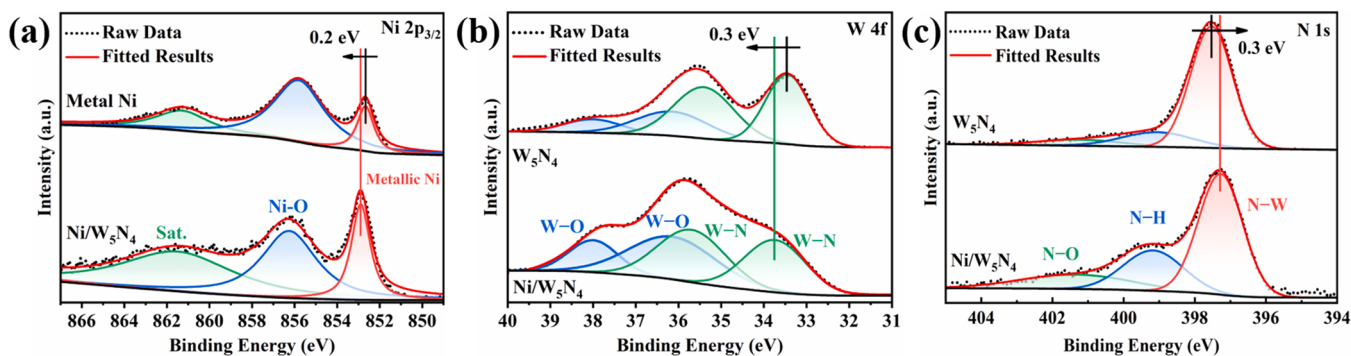


Fig. 3. (a) Ni 2p_{3/2}, (b) W 4f and (c) N 1s XPS spectra of the pure phase contrast samples and Ni/W_5N_4 catalyst.

shown in Fig. 4c, the potentials to achieve the current densities of 10 and 1000 mA cm⁻² were respectively required 1.51 and 1.88 V (vs. RHE). These potentials are much higher than those of UOR with about 160 and 280 mV, respectively. Here, OER potential at the current density of 10 mA cm⁻² was determined through the negative scanning segment of the CV curve to avoid interference by the redox peaks (Fig. S4a). The polarization curves under different electrolytes indicated that the UOR

takes place preferentially to the OER and is expected to replace the OER at the anode due to the possession of much lower potential.

The charge transfer resistance (R_{ct}) of the catalysts was measured by EIS to further probe the charge transfer kinetics. The obtained Nyquist plots (Fig. 4d) were fitted by Zview software. The results showed that Ni/W_5N_4 /NF possesses only 0.74 Ω of R_{ct} value, which is much lower than that of RuO_2 /NF (1.80 Ω), W_5N_4 /NF (2.15 Ω), hydrothermal

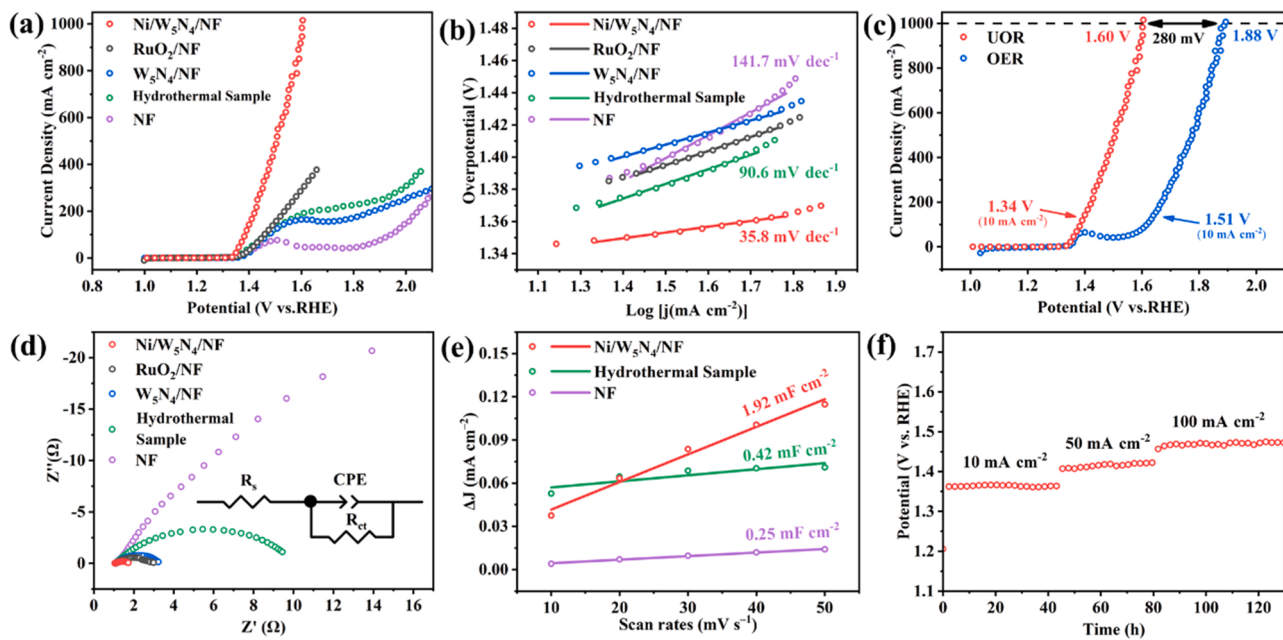


Fig. 4. (a) UOR polarization curves and (b) corresponding Tafel plots of the series of catalysts. (c) The comparison of polarization curves for the UOR and OER of Ni/W₅N₄/NF. (d) EIS Nyquist plots of the series of catalysts, with the insert showing the fitted equivalent circuit. (e) C_{dl} values of the series of catalysts. (f) The multistep CP curve of Ni/W₅N₄/NF for the UOR.

sample (9.16 Ω), and bare NF (100.7 Ω). This clearly indicated a faster electron transfer rate in the Ni/W₅N₄/NF sample [55]. The improvement of charge transferability of the Ni/W₅N₄/NF catalyst may be originated from the formation of the metal phase Ni and its intimate contact with the metal-like W₅N₄, as well as the formation of Janus-type charge distribution. In addition, the ECSA of the electrocatalyst can be evaluated by the calculated C_{dl} to reveal the number of surface active sites. Here, the CV method was performed in a nonaqueous aprotic KPF₆-CH₃CN electrolyte with different scan rates (Fig. S5-S7) to determine the C_{dl}, aiming at excluding the influence of hydration and protonation in an aqueous solution [47,48]. As shown in Fig. 4e, the C_{dl} value of Ni/W₅N₄/NF catalyst is 1.92 mF cm⁻², which is much higher than that of the hydrothermal sample (0.42 mF cm⁻²) and bare NF (0.25 mF cm⁻²). Compared with NF, the initial increase of C_{dl} of the hydrothermal sample is due to the in-situ growth of the Ni₄W₆O₂₁(OH)₂·4H₂O nano-microsphere during the hydrothermal process. And the further significant increase of C_{dl} after the nitridation process might be attributed to the dehydration reaction of the Ni₄W₆O₂₁(OH)₂·4H₂O precursor as well as the effective surface construction. Clearly, a higher C_{dl} of Ni/W₅N₄/NF catalyst indicates a larger ECSA, implying a more abundance of accessible active sites. To fairly evaluate the intrinsic activity of catalysts, we normalized the LSV curves using the ECSA values. Fig. S8 revealed that the Ni/W₅N₄/NF catalyst also possessed the higher ECSA-normalized current density at the same test potential, certifying the satisfied intrinsic activity of Ni/W₅N₄/NF catalyst over the contrast samples.

Long-term stability is another important parameter for practical application. The durability of Ni/W₅N₄/NF was evaluated by the multistep CP method under the current densities of 10, 50, and 100 mA cm⁻². As shown in Fig. 4f, the prepared self-supporting electrode displayed unobvious fluctuations of ± 4 mV, ± 10 mV, and ± 13 mV at the corresponding current densities, implying the excellent stability for total of 130 h of continuous UOR testing. The above results demonstrated that the Ni/W₅N₄/NF electrocatalyst possessed excellent UOR performance and stability in alkaline solution. After the testing, the electrocatalyst was further recharacterized by Raman spectroscopy, XPS, and HRTEM. Fig. S9 showed the comparison of the Raman results of the catalyst before and after the testing. Before the UOR process, the Raman peaks at

265, 697, and 802 cm⁻¹ can be identified as tungsten nitride species, which in agreement with the previous literature [56-59]. After the testing, these characteristic signals of tungsten nitride were disappeared and a pair of bands at 459 and 526 cm⁻¹ related to the bending and stretching vibrations of Ni-O in the NiOOH were observed [17,60,61]. In addition, the newly appeared bands at 326 and 832 cm⁻¹ associated with the W-O bond [62] may suggest the formation of tungsten oxyhydroxide species. These results were also confirmed by the XPS characterization. In Fig. S10a and S10b, the Ni 2p_{3/2} spectra showed the vanished metal Ni signal and the appeared Ni³⁺ signal of NiOOH, and the W 4f spectra also proved the converting from tungsten nitride to tungsten oxyhydroxide. The HRTEM results of the electrocatalyst after stability further revealed the occurrence of the surface reconstruction and the formation of the amorphous metal oxyhydroxide layer with a thickness of 5–15 nm (Fig. S11a). Even so, the heterojunction interfaces formed by Ni and W₅N₄ was still maintained inside the post-UOR catalyst (Fig. S11b), which should be ascribed to the protection of the amorphous layer along with the structural stability of the Mott-Schottky heterostructure [63,64]. Such results certified that surface of Ni/W₅N₄/NF catalyst reconstructed into the active nickel tungsten oxyhydroxides, which may act as the catalytically active phase for providing UOR active sites to greatly enhance the catalytic activity. This is consistent with previous reports about the UOR catalysts [32,36,38].

Encouraged by the outperforming UOR activity, we further investigated the HER capability of Ni/W₅N₄/NF catalyst in 1 M KOH. The results (Fig. 5a) showed that the Mott-Schottky heterojunction catalyst also exhibits excellent catalytic performance for the HER. The Ni/W₅N₄/NF catalyst requires an overpotential of only 25 mV to achieve a current density of 10 mA cm⁻², which is superior to all contrast samples and even better than the commercial Pt/C catalyst (32 mV). Impressively, it only needs an overpotential of 291 mV to handle a large current density of 1000 mA cm⁻². Here, the HER performance of the Ni/W₅N₄/NF electrocatalyst tested in the electrolytes with and without urea was nearly identical, demonstrating the presence of the urea in the electrolyte would not affect the HER performance of the catalyst (Fig. 5b). Furthermore, The Ni/W₅N₄/NF catalyst also showed satisfying stability for HER in the electrolyte of the 1 M KOH with 0.5 M urea. As shown in Fig. 5b, the current fluctuations are only ± 2 and ± 7 mV during 50 h of

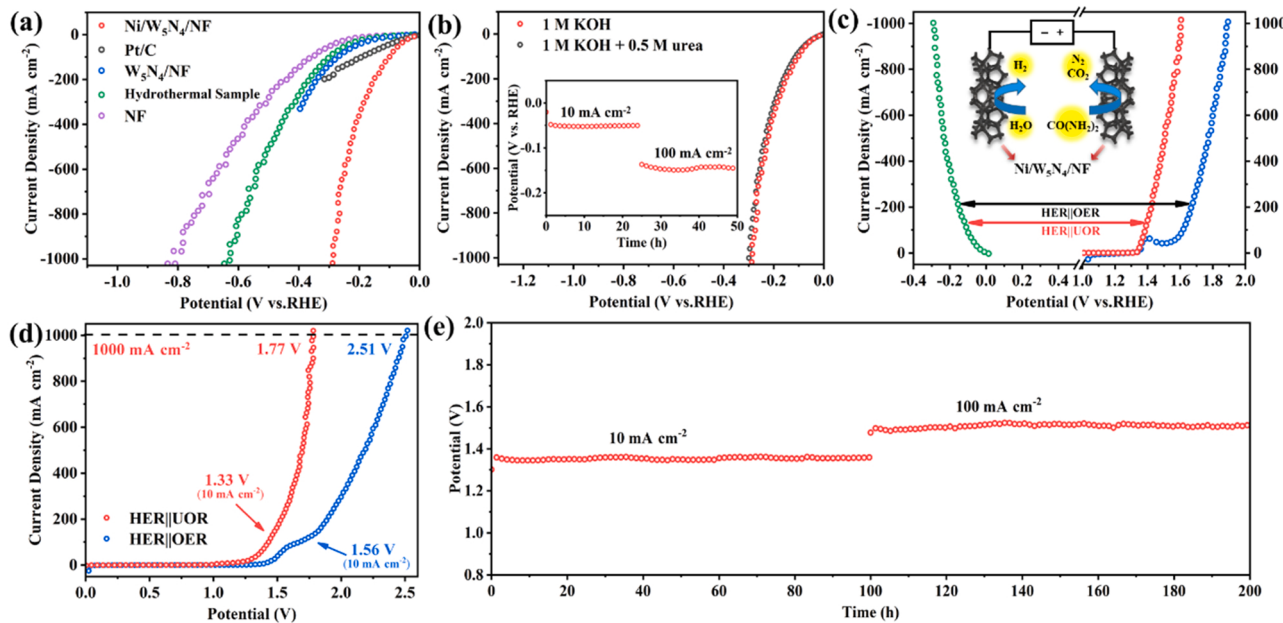


Fig. 5. (a) The HER polarization curves of the series of catalysts. (b) The polarization curves of Ni/W₅N₄/NF in the 1 M KOH electrolyte with and without 0.5 M urea. (c) The polarization curves of the Ni/W₅N₄/NF catalyst for HER, UOR, and OER, with the insert showing an illustrative schematic of the urea-assisted water electrolysis system assembled by the Ni/W₅N₄/NF electrodes. (d) The polarization curves of Ni/W₅N₄/NF in HER||UOR and HER||OER coupling systems. (e) The two-step CP curve of the urea-assisted hydrogen production system.

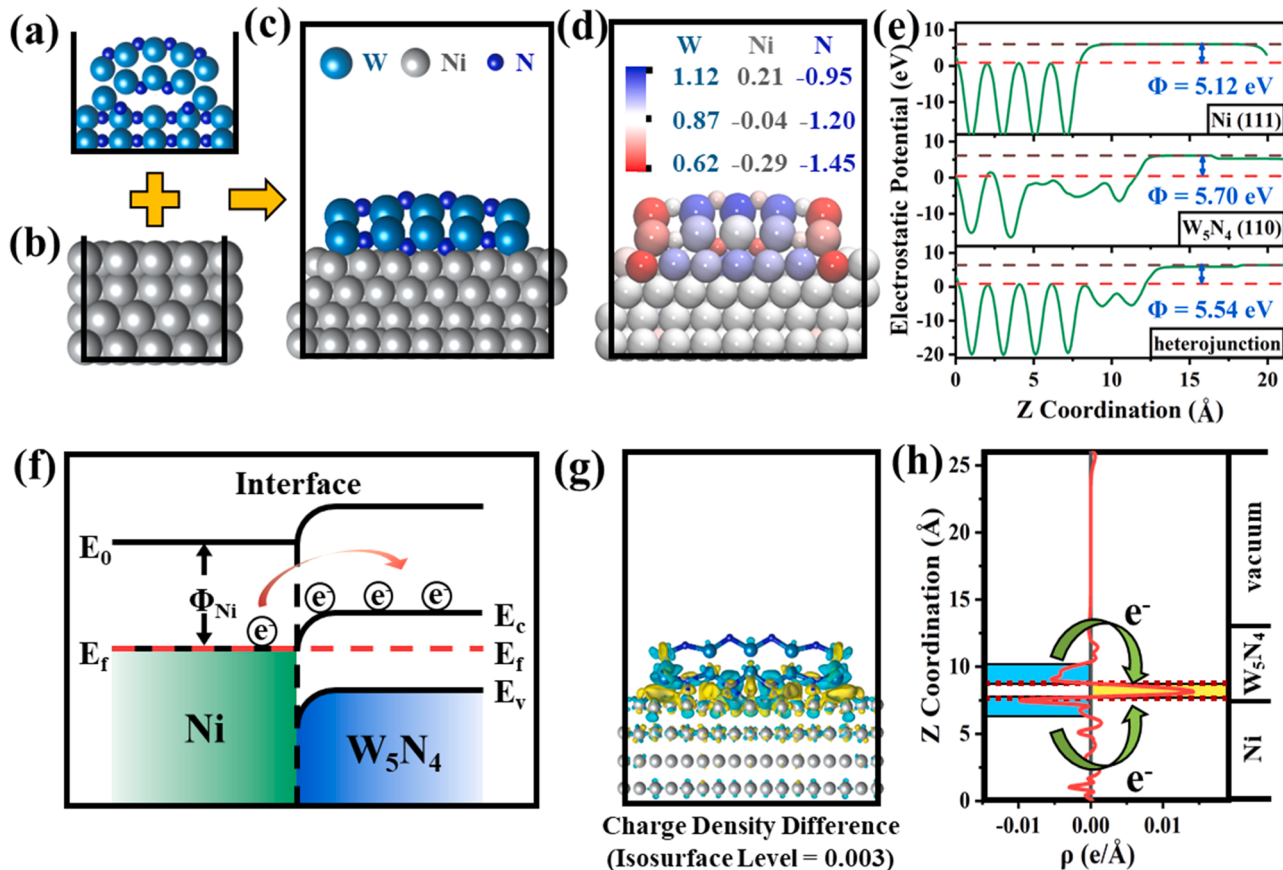


Fig. 6. Calculated geometries of (a) Ni (111), (b) W₅N₄ (100), and (c) Mott-Schottky heterojunction. (d) The structure diagram of atomic Bader Charge coloring for the Mott-Schottky heterojunction. (e) The electrostatic potential for the corresponding geometries. (f) Energy band diagram of metallic Ni and W₅N₄ with Mott-Schottky interface after Schottky contact. (g) The CDD image of the Mott-Schottky heterojunction formed from Ni (111) and W₅N₄ (100) (cyan stands for holes and yellow for electrons). (h) Planar-Average of CDD along the Z direction of the Mott-Schottky heterojunction formed from Ni (111) and W₅N₄ (100).

long-term testing at the current densities of 10 and 1000 mA cm⁻², respectively. The HRTEM images of the electrocatalyst after the HER stability also showed the interfaces remained well after the stability test (Fig. S12), revealing the favorable structural stability of the Ni/W₅N₄ Mott-Schottky heterostructure. The excellent HER performance of the Ni/W₅N₄/NF catalyst highlighted the key role of the Mott-Schottky heterostructure, which could accelerate the electron redistribution at the heterointerface and significantly enhanced the intrinsic catalytic activity for HER.

To further explore the mechanism of the electron redistribution at the Mott-Schottky heterojunction, the density functional theory (DFT) calculations of the established geometry were performed. In the established geometry, the pure phase of Ni and W₅N₄ appeared as the surface of 4 atomic layers of Ni (111) and W₅N₄ (100), respectively (Figs. 6a and 6b). Then two atomic layers of W₅N₄ (100) were placed on the four atomic layers of the Ni (111) surface to simulate the W₅N₄/Ni heterostructure (Fig. 6c). To explore the valence states of elements in the heterostructure and preliminarily study the direction of electron transfer, Bader Charge were calculated and the corresponding valence states were colored into the structure. As shown in Fig. 6d, the red spheres represent the atoms of lower valence, while blue spheres denote the atoms of higher valence. It could be seen that there were two N atoms with lower valence states in the heterostructure, suggesting that these N atoms accepted electrons from the surrounding atoms. Here, the valence state of the W atoms both on the left and right sides were significantly lower than the valence state of the W atoms in the middle, which may be caused by the fact that the four W atoms at sides only bond with one N atom. The Ni atoms adjacent to these W atoms also exhibited the similar situation, which should be attributed to the induction effect of the surrounding atoms. In summary, the potential gradients should exist in the X-axis, Y-axis, and Z-axis directions in the Mott-Schottky heterojunction. To further study the origin of electron transfer, the work functions of Ni (111), W₅N₄ (110), and Mott-Schottky heterojunction were calculated. According to the current theories, the work function (ϕ) is the minimum energy required for an electron to escape from the Fermi level to the vacuum level, it can be expressed as the following equation:

$$\Phi = E(\text{Vacuum}) - E(\text{Fermi}) \quad (4)$$

where $E(\text{Vacuum})$ and $E(\text{Fermi})$ are the electrostatic potentials of vacuum energy level and Fermi energy level, respectively. Fig. 6e showed the calculated work functions of metallic Ni (5.12 eV), W₅N₄ (5.70 eV), and the Mott-Schottky heterojunction formed by the two phases (5.54 eV). Since the work function of Ni is lower than that of W₅N₄, the two phases possess the essential terms to form the Mott-Schottky heterojunction [65,66]. Upon the formation of the Schottky contact, the work function difference would spontaneously drive electron transfer from Ni to W₅N₄, until the establishment of the built-in electric field and the realization of work function equilibrium, as shown in Fig. 6f. The established built-in electric field could accelerate the electron transfer and enhance the electronic conductivity. The electron redistribution could be further demonstrated by the charge density difference (CDD) (Fig. 6g) and the corresponding planar-averaged CDD along the Z direction (Fig. 6h) [67,68]. The calculation method of CDD can be denoted as the following equation:

$$\rho = \rho(\text{Mott-Schottky heterojunction}) - \rho(\text{Ni}) - \rho(\text{W}_5\text{N}_4) \quad (5)$$

where the $\rho(\text{Mott-Schottky heterojunction})$, $\rho(\text{Ni})$, and $\rho(\text{W}_5\text{N}_4)$ represent the charge densities of the corresponding structures, respectively. Fig. 6g showed an obvious aggregation of electrons at the heterointerface. This indicated the existence of electron transfer from Ni to W₅N₄ in the heterostructure, which is in agree well with the XPS results. From Fig. 6h, it can be found that the N atomic layer in contact with the Ni phase absorbed electrons from both the upper and lower directions. Such the massive electron redistribution can certainly optimize the adsorption/desorption of intermediates, and facilitate the adsorption

and activation of H₂O molecules, thereby significantly accelerating the whole HER process [42,44].

Owing to the excellent UOR and HER activities of Ni/W₅N₄/NF, the energy-saving urea-assisted water electrolysis system was established using the Ni/W₅N₄/NF electrodes both as the cathode and anode (Fig. 5c). As a comparison, the water splitting performance (OER and HER) of this two-electrode system in 1 M KOH was also tested. Fig. 5d showed the urea electrolysis system with UOR as anode and HER as cathode combination only needs the cell voltages of 1.33 and 1.77 V to reach the current densities of 10 and 1000 mA cm⁻², respectively. In comparison with the water electrolysis cell (1.56 and 2.51 V at 10 and 1000 mA cm⁻², respectively), the urea-assisted hydrogen production system presented a clear performance advantage. Additionally, the prolonged two-step CP test of the urea-assisted hydrogen production system was performed. Fig. 5e revealed a negligible change of the performance of the system after continuous electrolysis for 200 h, highlighting the excellent stability of the urea-assisted hydrogen production system. The robust stability of the targeted electrocatalyst might be associated with the successful construction of the Mott-Schottky heterojunction. Such a structure maintained the lattice orders and structural integrality and then gave rise to the greatly improved stability of the catalyst.

4. Conclusions

In conclusion, a Ni/W₅N₄ Mott-Schottky heterojunction catalyst supported on NF was synthesized by a facile hydrothermal method followed by thermal nitridation treatment. Benefiting from the surface reconstruction, high electrochemically active surface area and the improvement of charge transferability, the Ni/W₅N₄/NF catalyst exhibits high and stable electrocatalytic activity towards UOR. Meanwhile, the Janus electron distribution at the Mott-Schottky heterointerface endowed the catalyst with outstanding electrocatalytic performance towards the HER. In particular, the urea-assisted electrolysis cell using Ni/W₅N₄/NF as the bifunctional electrodes only needs the cell voltages of 1.33 and 1.77 V to deliver the current densities of 10 and 1000 mA cm⁻², respectively. These results suggested that the metal/TMN_s Mott-Schottky heterostructure materials may act as promising bifunctional catalysts for urea-assisted hydrogen production.

CRediT authorship contribution statement

Yumin Zhou: Methodology, Investigation, Data curation, Writing – original draft. **Bingxian Chu:** Data curation, DFT calculation, Visualization. **Zhengjian Sun:** Investigation, Validation. **Lihui Dong:** Project administration, Supervision. **Fan Wang:** Resources. **Bin Li:** Resources, Supervision. **Minguang Fan:** Funding acquisition, Supervision. **Zhengjun Chen:** Conceptualization, Writing – review & editing, Funding acquisition, Supervision.

Declaration of Competing Interest

The authors declare that they have no known competing financial interests or personal relationships that could have appeared to influence the work reported in this paper.

Data availability

Data will be made available on request.

Acknowledgements

This work was supported by National Natural Science Foundation of China [Grant numbers 21968002, 21763003, 22062002] and the Startup Fund of Guangxi University [Grant number A3040051014]. The DFT calculations were supported by the high-performance computing

platform of Guangxi University.

Appendix A. Supporting information

Supplementary data associated with this article can be found in the online version at [doi:10.1016/j.apcatb.2022.122168](https://doi.org/10.1016/j.apcatb.2022.122168).

References

- [1] J.A. Turner, Sustainable hydrogen production, *Science* 305 (2004) 972–974, <https://doi.org/10.1126/science.1103197>.
- [2] Z.W. Seh, J. Kibsgaard, C.F. Dickens, I. Chorkendorff, J.K. Nørskov, T.F. Jaramillo, Combining theory and experiment in electrocatalysis: insights into materials design, *Science* 355 (2017) eaad4998, <https://doi.org/10.1126/science.aad4998>.
- [3] P. Wang, T. Wang, R. Qin, Z. Pu, C. Zhang, J. Zhu, D. Chen, D. Feng, Z. Kou, S. Mu, J. Wang, Swapping catalytic active sites from cationic Ni to anionic S in nickel sulfide enables more efficient alkaline hydrogen generation, *Adv. Energy Mater.* 12 (2022), 2103359, <https://doi.org/10.1002/aenm.202103359>.
- [4] J. Kibsgaard, I. Chorkendorff, Considerations for the scaling-up of water splitting catalysts, *Nat. Energy* 4 (2019) 430–433, <https://doi.org/10.1038/s41560-019-0407-1>.
- [5] L. Huang, D. Chen, G. Luo, Y.R. Lu, C. Chen, Y. Zou, C.L. Dong, Y. Li, S. Wang, Zirconium-regulation-induced bifunctionality in 3D cobalt-iron oxide nanosheets for overall water splitting, *Adv. Mater.* 31 (2019), e1901439, <https://doi.org/10.1002/adma.201901439>.
- [6] I. Roger, M.A. Shipman, M.D. Symes, Earth-abundant catalysts for electrochemical and photoelectrochemical water splitting, *Nat. Rev. Chem.* 1 (2017) 0003, <https://doi.org/10.1038/s41570-016-0003>.
- [7] P. Wang, R. Qin, P. Ji, Z. Pu, J. Zhu, C. Lin, Y. Zhao, H. Tang, W. Li, S. Mu, Synergistic coupling of Ni nanoparticles with Ni₃C nanosheets for highly efficient overall water splitting, *Small* 16 (2020), e2001642, <https://doi.org/10.1002/smll.202001642>.
- [8] D. Zhao, Y. Pi, Q. Shao, Y. Feng, Y. Zhang, X. Huang, Enhancing oxygen evolution electrocatalysis via the intimate hydroxide–oxide interface, *ACS Nano* 12 (2018) 6245–6251, <https://doi.org/10.1021/acsnano.8b03141>.
- [9] Q. Shi, C. Zhu, D. Du, Y. Lin, Robust noble metal-based electrocatalysts for oxygen evolution reaction, *Chem. Soc. Rev.* 48 (2019) 3181–3192, <https://doi.org/10.1039/C8CS00671G>.
- [10] S.-K. Geng, Y. Zheng, S.-Q. Li, H. Su, X. Zhao, J. Hu, H.-B. Shu, M. Jaroniec, P. Chen, Q.-H. Liu, S.-Z. Qiao, Nickel ferrocyanide as a high-performance urea oxidation electrocatalyst, *Nat. Energy* 6 (2021) 904–912, <https://doi.org/10.1038/s41560-021-00899-2>.
- [11] R.P. Forslund, J.T. Mefford, W.G. Hardin, C.T. Alexander, K.P. Johnston, K. J. Stevenson, Nanostructured LaNiO₃ perovskite electrocatalyst for enhanced urea oxidation, *ACS Catal.* 6 (2016) 5044–5051, <https://doi.org/10.1021/acscatal.6b00487>.
- [12] Y. Li, X. Wei, L. Chen, J. Shi, Electrocatalytic hydrogen production trilogy, *Angew. Chem. Int. Ed.* 60 (2021) 19550–19571, <https://doi.org/10.1002/anie.202009854>.
- [13] X.F. Lu, S.L. Zhang, W.L. Sim, S. Gao, X.W.D. Lou, Phosphorized CoNi₂S₄ yolk-shell spheres for highly efficient hydrogen production via water and urea electrolysis, *Angew. Chem. Int. Ed.* 60 (2021) 22885–22891, <https://doi.org/10.1002/anie.202108563>.
- [14] C. Li, Y. Liu, Z. Zhuo, H. Ju, D. Li, Y. Guo, X. Wu, H. Li, T. Zhai, Local charge distribution engineered by Schottky heterojunctions toward urea electrolysis, *Adv. Energy Mater.* 8 (2018), 1801775, <https://doi.org/10.1002/aenm.201801775>.
- [15] Z.-Y. Yu, C.-C. Lang, M.-R. Gao, Y. Chen, Q.-Q. Fu, Y. Duan, S.-H. Yu, Ni–Mo–O nanorod-derived composite catalysts for efficient alkaline water-to-hydrogen conversion via urea electrolysis, *Energy Environ. Sci.* 11 (2018) 1890–1897, <https://doi.org/10.1039/c8ee00521d>.
- [16] L. Wang, Y. Zhu, Y. Wen, S. Li, C. Cui, F. Ni, Y. Liu, H. Lin, Y. Li, H. Peng, B. Zhang, Regulating the local charge distribution of Ni active sites for the urea oxidation reaction, *Angew. Chem. Int. Ed.* 60 (2021) 10577–10582, <https://doi.org/10.1002/anie.202010610>.
- [17] Z. Ji, Y. Song, S. Zhao, Y. Li, J. Liu, W. Hu, Pathway manipulation via Ni, Co, and V ternary synergism to realize high efficiency for urea electrocatalytic oxidation, *ACS Catal.* 12 (2021) 569–579, <https://doi.org/10.1021/acscatal.1c05190>.
- [18] Z. Wang, W. Liu, J. Bao, Y. Song, X. She, Y. Hua, G. Lv, J. Yuan, H. Li, H. Xu, Modulating electronic structure of ternary NiMoV LDH nanosheet array induced by doping engineering to promote urea oxidation reaction, *Chem. Eng. J.* 430 (2022), 133100, <https://doi.org/10.1016/j.cej.2021.133100>.
- [19] S. Ni, H. Qu, Z. Xu, X. Zhu, H. Xing, L. Wang, J. Yu, H. Liu, C. Chen, L. Yang, Interfacial engineering of the NiSe₂/FeSe₂ p–p heterojunction for promoting oxygen evolution reaction and electrocatalytic urea oxidation, *Appl. Catal. B Environ.* 299 (2021), 120638, <https://doi.org/10.1016/j.apcatb.2021.120638>.
- [20] S. Chen, J. Duan, A. Vasileff, S.Z. Qiao, Size fractionation of two-dimensional sub-nanometer thin manganese dioxide crystals towards superior urea electrocatalytic conversion, *Angew. Chem. Int. Ed.* 55 (2016) 3804–3808, <https://doi.org/10.1002/anie.201600387>.
- [21] H. Jiang, M. Sun, S. Wu, B. Huang, C.S. Lee, W. Zhang, Oxygen-incorporated NiMoP nanotube arrays as efficient bifunctional electrocatalysts for urea-assisted energy-saving hydrogen production in alkaline electrolyte, *Adv. Funct. Mater.* 31 (2021), 2104951, <https://doi.org/10.1002/adfm.202104951>.
- [22] D. Liu, T. Liu, L. Zhang, F. Qu, G. Du, A.M. Asiri, X. Sun, High-performance urea electrolysis towards less energy-intensive electrochemical hydrogen production using a bifunctional catalyst electrode, *J. Mater. Chem. A* 5 (2017) 3208–3213, <https://doi.org/10.1039/C6TA11127K>.
- [23] T. Yu, Q. Xu, J. Chen, G. Qian, X. Zhuo, H. Yang, S. Yin, Boosting urea-assisted water splitting by constructing sphere-flower-like NiSe₂–NiMoO₄ heterostructure, *Chem. Eng. J.* 449 (2022), 137791, <https://doi.org/10.1016/j.cej.2022.137791>.
- [24] C. Wang, H. Lu, Z. Mao, C. Yan, G. Shen, X. Wang, Bimetal Schottky heterojunction boosting energy-saving hydrogen production from alkaline water via urea electrocatalysis, *Adv. Funct. Mater.* 30 (2020), 2000556, <https://doi.org/10.1002/adfm.202000556>.
- [25] Y. Cheng, F. Liao, H. Dong, H. Wei, H. Geng, M. Shao, Engineering CoN/Ni(OH)₂ heterostructures with improved intrinsic interfacial charge transfer toward simultaneous hydrogen generation and urea-rich wastewater purification, *J. Power Sources* 480 (2020), 229151, <https://doi.org/10.1016/j.jpowsour.2020.229151>.
- [26] H. Sun, W. Zhang, J.-G. Li, Z. Li, X. Ao, K.-H. Xue, K.K. Ostrikov, J. Tang, C. Wang, Rh-engineered ultrathin NiFe-LDH nanosheets enable highly-efficient overall water splitting and urea electrolysis, *Appl. Catal. B Environ.* 284 (2021), 119740, <https://doi.org/10.1016/j.apcatb.2020.119740>.
- [27] K.R.G. Lim, A.D. Handoko, S.K. Nemani, B. Wyatt, H.Y. Jiang, J. Tang, B. Anasori, Z.W. Seh, Rational design of two-dimensional transition metal carbide/nitride (MXene) hybrids and nanocomposites for catalytic energy storage and conversion, *ACS Nano* 14 (2020) 10834–10864, <https://doi.org/10.1021/acsnano.0c05482>.
- [28] H. Wang, J. Li, K. Li, Y. Lin, J. Chen, L. Gao, V. Nicolosi, X. Xiao, J.M. Lee, Transition metal nitrides for electrochemical energy applications, *Chem. Soc. Rev.* 50 (2021) 1354–1390, <https://doi.org/10.1039/DCOS00415D>.
- [29] M. Li, X. Wu, K. Liu, Y. Zhang, X. Jiang, D. Sun, Y. Tang, K. Huang, G. Fu, Nitrogen vacancies enriched Ce-doped Ni₃N hierarchical nanosheets triggering highly-efficient urea oxidation reaction in urea-assisted energy-saving electrolysis, *J. Energy Chem.* 69 (2022) 506–515, <https://doi.org/10.1016/j.jechem.2022.01.031>.
- [30] R.-Q. Li, Q. Liu, Y. Zhou, M. Lu, J. Hou, K. Qu, Y. Zhu, O. Fontaine, 3D self-supported porous vanadium-doped nickel nitride nanosheet arrays as efficient bifunctional electrocatalysts for urea electrolysis, *J. Mater. Chem. A* 9 (2021) 4159–4166, <https://doi.org/10.1039/D0TA09473K>.
- [31] R.-Q. Li, X.-Y. Wan, B.-L. Chen, R.-Y. Cao, Q.-H. Ji, J. Deng, K.-G. Qu, X.-B. Wang, Y.-C. Zhu, Hierarchical Ni₃N/Ni_{0.2}Mo_{0.8}N heterostructure nanorods arrays as efficient electrocatalysts for overall water and urea electrolysis, *Chem. Eng. J.* 409 (2021), 128240, <https://doi.org/10.1016/j.cej.2020.128240>.
- [32] F. Cai, L. Liao, Y. Zhao, D. Li, J. Zeng, F. Yu, H. Zhou, Large-current-stable bifunctional nanoporous Fe-rich nitride electrocatalysts for highly efficient overall water and urea splitting, *J. Mater. Chem. A* 9 (2021) 10199–10207, <https://doi.org/10.1039/DITA00144B>.
- [33] B.K. Boggs, R.L. King, G.G. Botte, Urea electrolysis: direct hydrogen production from urine, *Chem. Commun.* (2009) 4859–4861, <https://doi.org/10.1039/B905974A>.
- [34] R.K. Singh, K. Rajavelu, M. Montag, A. Schechter, Advances in catalytic electrooxidation of urea: a review, *Energy Technol.* 9 (2021), 2100017, <https://doi.org/10.1002/ente.202010017>.
- [35] Q. He, Y. Wan, H. Jiang, Z. Pan, C. Wu, M. Wang, X. Wu, B. Ye, P.M. Ajayan, L. Song, Nickel vacancies boost reconstruction in nickel hydroxide electrocatalyst, *ACS Energy Lett.* 3 (2018) 1373–1380, <https://doi.org/10.1021/acsenergylett.8b00515>.
- [36] X. Liu, K. Ni, B. Wen, R. Guo, C. Niu, J. Meng, Q. Li, P. Wu, Y. Zhu, X. Wu, L. Mai, Deep reconstruction of nickel-based precatalysts for water oxidation catalysis, *ACS Energy Lett.* 4 (2019) 2585–2592, <https://doi.org/10.1021/acsenergylett.9b01922>.
- [37] L. Liu, Z. Zhou, C. Peng, Sonochemical intercalation synthesis of nano γ-nickel oxyhydroxide: structure and electrochemical properties, *Electrochim. Acta* 54 (2008) 434–441, <https://doi.org/10.1016/j.electacta.2008.07.055>.
- [38] W. Sun, J. Li, W. Gao, L. Kang, F. Lei, J. Xie, Recent advances in the pre-oxidation process in electrocatalytic urea oxidation reactions, *Chem. Commun.* 58 (2022) 2430–2442, <https://doi.org/10.1039/D1CC06290E>.
- [39] H. Yang, B. Wang, S. Kou, G. Lu, Z. Liu, Mott–Schottky heterojunction of Co/Co₂P with built-in electric fields for bifunctional oxygen electrocatalysis and zinc-air battery, *Chem. Eng. J.* 425 (2021), 131589, <https://doi.org/10.1016/j.cej.2021.131589>.
- [40] P. Wang, Z. Pu, W. Li, J. Zhu, C. Zhang, Y. Zhao, S. Mu, Coupling NiSe₂–Ni₂P heterostructure nanowrinkles for highly efficient overall water splitting, *J. Catal.* 377 (2019) 600–608, <https://doi.org/10.1016/j.jcat.2019.08.005>.
- [41] Q. Zhang, F. Luo, X. Long, X. Yu, K. Qu, Z. Yang, N, P doped carbon nanotubes confined WN–Ni Mott–Schottky heterogenous electrocatalyst for water splitting and rechargeable zinc-air batteries, *Appl. Catal. B Environ.* 298 (2021), 120511, <https://doi.org/10.1016/j.apcatb.2021.120511>.
- [42] C. Gu, G. Zhou, J. Yang, H. Pang, M. Zhang, Q. Zhao, X. Gu, S. Tian, J. Zhang, L. Xu, Y. Tang, Ni₃S/MoS₂ Mott–Schottky heterojunction-induced local charge redistribution for high-efficiency urea-assisted energy-saving hydrogen production, *Chem. Eng. J.* 443 (2022), 136321, <https://doi.org/10.1016/j.cej.2022.136321>.
- [43] H. Luo, J. Barrio, N. Sunny, A. Li, L. Steier, N. Shah, I.E.L. Stephens, M.M. Titirici, Progress and perspectives in photo- and electrochemical-oxidation of biomass for sustainable chemicals and hydrogen production, *Adv. Energy Mater.* 11 (2021), 2101180, <https://doi.org/10.1002/aenm.202101180>.
- [44] L. Peng, L. Su, X. Yu, R. Wang, X. Cui, H. Tian, S. Cao, B.Y. Xia, J. Shi, Electron redistribution of ruthenium-tungsten oxides Mott–Schottky heterojunction for enhanced hydrogen evolution, *Appl. Catal. B Environ.* 308 (2022), 121229, <https://doi.org/10.1016/j.apcatb.2022.121229>.

[45] X. Ji, Y. Zhang, Z. Ma, Y. Qiu, Oxygen vacancy-rich Ni/NiO@NC nanosheets with Schottky heterointerface for efficient urea oxidation reaction, *ChemSusChem* 13 (2020) 5004–5014, <https://doi.org/10.1002/cssc.202001185>.

[46] Y. Zhou, R. Li, L. Dong, S. Yin, B. Chu, Z. Chen, J. Wang, B. Li, M. Fan, Heterointerface and defect dual engineering in a superhydrophilic $\text{Ni}_2\text{P}/\text{WO}_{2.83}$ microsphere for boosting alkaline hydrogen evolution reaction at high current density, *ACS Appl. Mater. Interfaces* 14 (2022) 18816–18824, <https://doi.org/10.1021/acsami.2c01208>.

[47] Y. Yoon, B. Yan, Y. Surendranath, Suppressing ion transfer enables versatile measurements of electrochemical surface area for intrinsic activity comparisons, *J. Am. Chem. Soc.* 140 (2018) 2397–2400, <https://doi.org/10.1021/jacs.7b10966>.

[48] G.-X. Cao, Z.-J. Chen, H. Yin, L.-Y. Gan, M.-J. Zang, N. Xu, P. Wang, Investigation of the correlation between the phase structure and activity of Ni–Mo–O derived electrocatalysts for the hydrogen evolution reaction, *J. Mater. Chem. A* 7 (2019) 10338–10345, <https://doi.org/10.1039/C9TA00899C>.

[49] S. Qin, Y. Duan, X.L. Zhang, L.R. Zheng, F.Y. Gao, P.P. Yang, Z.Z. Niu, R. Liu, Y. Yang, X.S. Zheng, J.F. Zhu, M.R. Gao, Ternary nickel-tungsten-copper alloy rivals platinum for catalyzing alkaline hydrogen oxidation, *Nat. Commun.* 12 (2021) 2686, <https://doi.org/10.1038/s41467-021-22996-2>.

[50] L. Fan, P.F. Liu, X. Yan, L. Gu, Z.Z. Yang, H.G. Yang, S. Qiu, X. Yao, Atomically isolated nickel species anchored on graphitized carbon for efficient hydrogen evolution electrocatalysis, *Nat. Commun.* 7 (2016) 10667, <https://doi.org/10.1038/ncomms10667>.

[51] W. Luo, Y. Wang, L. Luo, S. Gong, M. Wei, Y. Li, X. Gan, Y. Zhao, Z. Zhu, Z. Li, Single-atom and bimetallic nanoalloy supported on nanotubes as a bifunctional electrocatalyst for ultrahigh-current-density overall water splitting, *ACS Catal.* 12 (2022) 1167–1179, <https://doi.org/10.1021/acscatal.1c04454>.

[52] F. Ma, S. Wang, X. Gong, X. Liu, Z. Wang, P. Wang, Y. Liu, H. Cheng, Y. Dai, Z. Zheng, B. Huang, Highly efficient electrocatalytic hydrogen evolution coupled with upcycling of microplastics in seawater enabled via $\text{Ni}_3\text{N}/\text{W}_5\text{N}_4$ janus nanostructures, *Appl. Catal. B Environ.* 307 (2022), 121198, <https://doi.org/10.1016/j.apcatb.2022.121198>.

[53] S. Tan, B.M. Tackett, Q. He, J.H. Lee, J.G. Chen, S.S. Wong, Synthesis and electrocatalytic applications of flower-like motifs and associated composites of nitrogen-enriched tungsten nitride (W_2N_3), *Nano Res.* 13 (2020) 1434–1443, <https://doi.org/10.1007/s12274-020-2687-y>.

[54] B. Ren, D. Li, Q. Jin, H. Cui, C. Wang, A self-supported porous WN nanowire array: an efficient 3D electrocatalyst for the hydrogen evolution reaction, *J. Mater. Chem. A* 5 (2017) 19072–19078, <https://doi.org/10.1039/C7TA04923D>.

[55] X.L. Zhang, P.P. Yang, Y.R. Zheng, Y. Duan, S.J. Hu, T. Ma, F.Y. Gao, Z.Z. Niu, Z. Z. Wu, S. Qin, L.P. Chi, X. Yu, R. Wu, C. Gu, C.M. Wang, X.S. Zheng, X. Zheng, J. F. Zhu, M.R. Gao, An efficient Turing-type $\text{Ag}_2\text{Se}-\text{CoSe}_2$ multi-interfacial oxygen-evolving electrocatalyst, *Angew. Chem. Int. Ed.* 60 (2021) 6553–6560, <https://doi.org/10.1002/anie.202017016>.

[56] L. Villaseca, B. Moreno, I. Lorite, J.R. Jurado, E. Chinarro, Synthesis and characterization of tungsten nitride (W_2N) from WO_3 and H_2WO_4 to be used in the electrode of electrochemical devices, *Ceram. Int.* 41 (2015) 4282–4288, <https://doi.org/10.1016/j.ceramint.2014.11.114>.

[57] V. Chakrapani, J. Thangala, M.K. Sunkara, WO_3 and W_2N nanowire arrays for photoelectrochemical hydrogen production, *Int. J. Hydrog. Energy* 34 (2009) 9050–9059, <https://doi.org/10.1016/j.ijhydene.2009.09.031>.

[58] M. Zhang, Y. Qiu, Y. Han, Y. Guo, F. Cheng, Three-dimensional tungsten nitride nanowires as high performance anode material for lithium ion batteries, *J. Power Sources* 322 (2016) 163–168, <https://doi.org/10.1016/j.jpowsour.2016.04.049>.

[59] B. Wicher, R. Chodun, K. Nowakowska-Langier, M. Trzciński, L. Skowroński, S. Okrasa, R. Minikayev, M.K. Naparty, K. Zduńek, Chemical and structural characterization of tungsten nitride (WN_x) thin films synthesized via Gas Injection Magnetron Sputtering technique, *Vacuum* 165 (2019) 266–273, <https://doi.org/10.1016/j.vacuum.2019.04.020>.

[60] L. Sha, T. Liu, K. Ye, K. Zhu, J. Yan, J. Yin, G. Wang, D. Cao, A heterogeneous interface on $\text{NiS}@\text{Ni}_3\text{S}_2/\text{NiMoO}_4$ heterostructures for efficient urea electrolysis, *J. Mater. Chem. A* 8 (2020) 18055–18063, <https://doi.org/10.1039/D0TA04944A>.

[61] X. Gao, X. Liu, W. Zang, H. Dong, Y. Pang, Z. Kou, P. Wang, Z. Pan, S. Wei, S. Mu, J. Wang, Synergizing in-grown $\text{Ni}_3\text{N}/\text{Ni}$ heterostructured core and ultrathin Ni_3N surface shell enables self-adaptive surface reconfiguration and efficient oxygen evolution reaction, *Nano Energy* 78 (2020), 105355, <https://doi.org/10.1016/j.nanoen.2020.105355>.

[62] E.I. Ross-Medgaarden, I.E. Wachs, Structural determination of bulk and surface tungsten oxides with UV-vis diffuse reflectance spectroscopy and Raman spectroscopy, *J. Phys. Chem. C* 111 (2007) 15089–15099, <https://doi.org/10.1021/jp074219c>.

[63] P. Chen, K. Xu, Z. Fang, Y. Tong, J. Wu, X. Lu, X. Peng, H. Ding, C. Wu, Y. Xie, Metallic Co_4N porous nanowire arrays activated by surface oxidation as electrocatalysts for the oxygen evolution reaction, *Angew. Chem. Int. Ed.* 54 (2015) 14710–14714, <https://doi.org/10.1002/anie.201506480>.

[64] S. Ligani Fereja, P. Li, Z. Zhang, J. Guo, Z. Fang, Z. Li, S. He, W. Chen, W-doping induced abundant active sites in a 3D $\text{NiS}_2/\text{MoO}_2$ heterostructure as an efficient electrocatalyst for urea oxidation and hydrogen evolution reaction, *Chem. Eng. J.* 432 (2022), 134274, <https://doi.org/10.1016/j.cej.2021.134274>.

[65] Q. Zhang, B. Liu, L. Li, Y. Ji, C. Wang, L. Zhang, Z. Su, Maximized Schottky effect: the ultrafine $\text{V}_2\text{O}_3/\text{Ni}$ heterojunctions repeatedly arranging on monolayer nanosheets for efficient and stable water-to-hydrogen conversion, *Small* 17 (2021), e2005769, <https://doi.org/10.1002/smll.202005769>.

[66] Y. Sun, T. Liu, Z. Li, A. Meng, G. Li, L. Wang, S. Li, Morphology and interfacial charge regulation strategies constructing 3D flower-like $\text{Co}@\text{CoP}_2$ heterostructure electrocatalyst for efficient overall water splitting, *Chem. Eng. J.* 433 (2022), 133684, <https://doi.org/10.1016/j.cej.2021.133684>.

[67] X.L. Zhang, X. Su, Y.R. Zheng, S.J. Hu, L. Shi, F.Y. Gao, P.P. Yang, Z.Z. Niu, Z. Z. Wu, S. Qin, R. Wu, Y. Duan, C. Gu, X.S. Zheng, J.F. Zhu, M.R. Gao, Strongly coupled cobalt diselenide monolayers for selective electrocatalytic oxygen reduction to H_2O_2 under acidic conditions, *Angew. Chem. Int. Ed.* 60 (2021) 26922–26931, <https://doi.org/10.1002/anie.202111075>.

[68] Y. Yang, F.Y. Gao, X.L. Zhang, S. Qin, L.R. Zheng, Y.H. Wang, J. Liao, Q. Yang, M. R. Gao, Suppressing electron back-donation for a highly CO-tolerant fuel cell anode catalyst via cobalt modulation, *Angew. Chem. Int. Ed.* (2022), e202208040, <https://doi.org/10.1002/anie.202208040>.